

## Research Article

# Influence of Propeller Slipstream on the Flow Field of S-Shaped Intake

Shuili Ren  and Peiqing Liu

Beijing University of Aeronautics and Astronautics, Beijing 100191, China

Correspondence should be addressed to Shuili Ren; renshuili@hotmail.com

Received 22 April 2021; Revised 22 August 2021; Accepted 9 October 2021; Published 27 October 2021

Academic Editor: Adel Ghenaïet

Copyright © 2021 Shuili Ren and Peiqing Liu. This is an open access article distributed under the Creative Commons Attribution License, which permits unrestricted use, distribution, and reproduction in any medium, provided the original work is properly cited.

For turboprop engine, the S-shaped intake affects the engine performance and the propeller is not far in front of the inlet of the S-shaped intake, so the slipstream inevitably affects the flow field in the S-shaped intake and the engine performance. Here, an S-shaped intake with/without propeller is studied by solving Reynolds-averaged Navier-Stokes equation employed SST  $k-\omega$  turbulence model. The results are presented as time-averaged results and transient results. By comparing the flow field in S-shaped intake with/without propeller, the transient results show that total pressure recovery coefficient and distortion coefficient on the AIP section vary periodically with time. The time-averaged results show that the influence of propeller slipstream on the performance of S-shaped intake is mainly circumferential interference and streamwise interference. Circumferential interference mainly affects the secondary flow in the S-shaped intake and then affects the airflow uniformity; the streamwise interference mainly affects the streamwise flow separation in the S-shaped intake and then affects the total pressure recovery. The total pressure recovery coefficient on the AIP section for the S-shaped intake with propeller is 1%-2.5% higher than that for S-shaped intake without propeller, and the total pressure distortion coefficient on the AIP section for the S-shaped intake with propeller is 1%-12% higher than that for the S-shaped intake without propeller. However, compared with the free stream flow velocity ( $Ma = 0.527$ ), the influence of the propeller slipstream belongs to the category of small disturbance, which is acceptable for engineering applications.

## 1. Introduction

The S-shaped intake has several advantages: (1) its structure is compact [1]; (2) it can decrease the propulsion system resistance [2]; (3) it can decrease the radar sweeping area and improve the aircraft stealth performance [3–5]. In view of the above advantages, it has been widely applied in modern commercial aircraft and military aircraft, such as Boeing 727, General Dynamics F-16, and McDonald-Douglas F-18 [6–8].

The ideal S-shaped intake can effectively decrease the airflow velocity, increase the airflow static pressure, and provide uniform airflow for engine compressor [7]. However, the geometric characteristic of S-shaped intake is that the centerline has curvature, and the cross section increases in main flow direction [7, 9, 10]. The centerline curvature leads to a pair of counter-rotating vortices, and increase cross section causes streamwise flow separation [11, 12]. The com-

plex flow phenomena increases the airflow total pressure loss and distortion on the Aerodynamic Interface Plane (AIP), which not only drops the engine performance, but also leads to diversified troubles [7].

Numerous researchers have studied the flow field in the S-shaped intake. Wellborn et al. [7] studied the subsonic compressible flow through a diffused S-duct. They observed the streamwise flow separation and the counter-rotating vortices in the S-duct and provided standard verification data for Computational Fluid Dynamics (CFD). Wendt and Reichert [8] have conducted an experimental study on vortex ingestion in a diffusing S-shaped intake. They reported that the appropriate vortex ingestion can inhibit flow separation in the S-shaped intake. Fiola and Agarwal [13] have studied numerically the diffusion S-duct, employing different turbulence models in their research. It is found that the SST  $k-\omega$  turbulence model has a better ability to capture

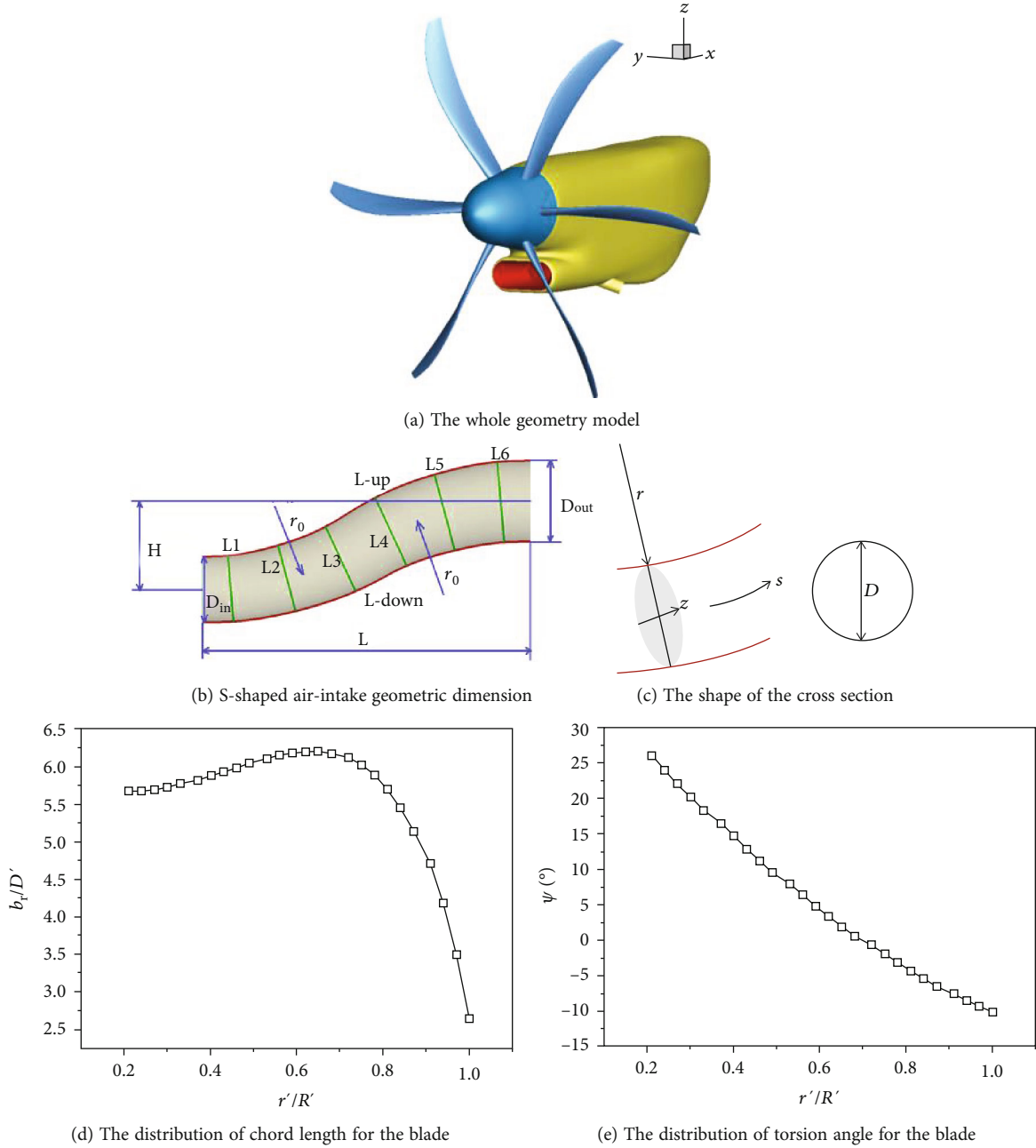


FIGURE 1: The computational model in the present study.

TABLE 1: Geometric dimensions of computational model.

Parameter	Value	Parameter	Value
$D_{in}$ , mm	266.3	$r_0$ , mm	1330.8
$D_{out}$ , mm	328	$H$ , mm	359.5
$L$ , mm	1330.8	$D'$ , mm	4000

the flow field in the S-duct. Gil-Prieto et al. [14] have carried out a delayed detached-eddy simulation (DDES) on the flow field in S-duct. They demonstrated that DDES simulation has good ability to capture the unsteady characteristics for the highly turbulent flow field in S-duct.

In a word, the literatures mentioned above show that many achievements have been made in the study on the single S-shaped intake. However, the propeller effect on the flow field in S-shaped intake of is rarely studied. As the lip of the turboprop engine intake is close to the propeller rotating plane [15–17], the propeller periodically pushes air into the intake, which inevitably affects the engine performance. McDill [16] carried out a test in the NASA Lewis Research Center wind tunnel to explore the impact of the design parameters (lip thickness, cross section geometry, throat design Mach number, and shaft fairing shape) on the S-shaped intake performance. His results indicated the design parameters (lip thickness and shaft fairing cross section) could be optimized to prevent excessive distortion on the

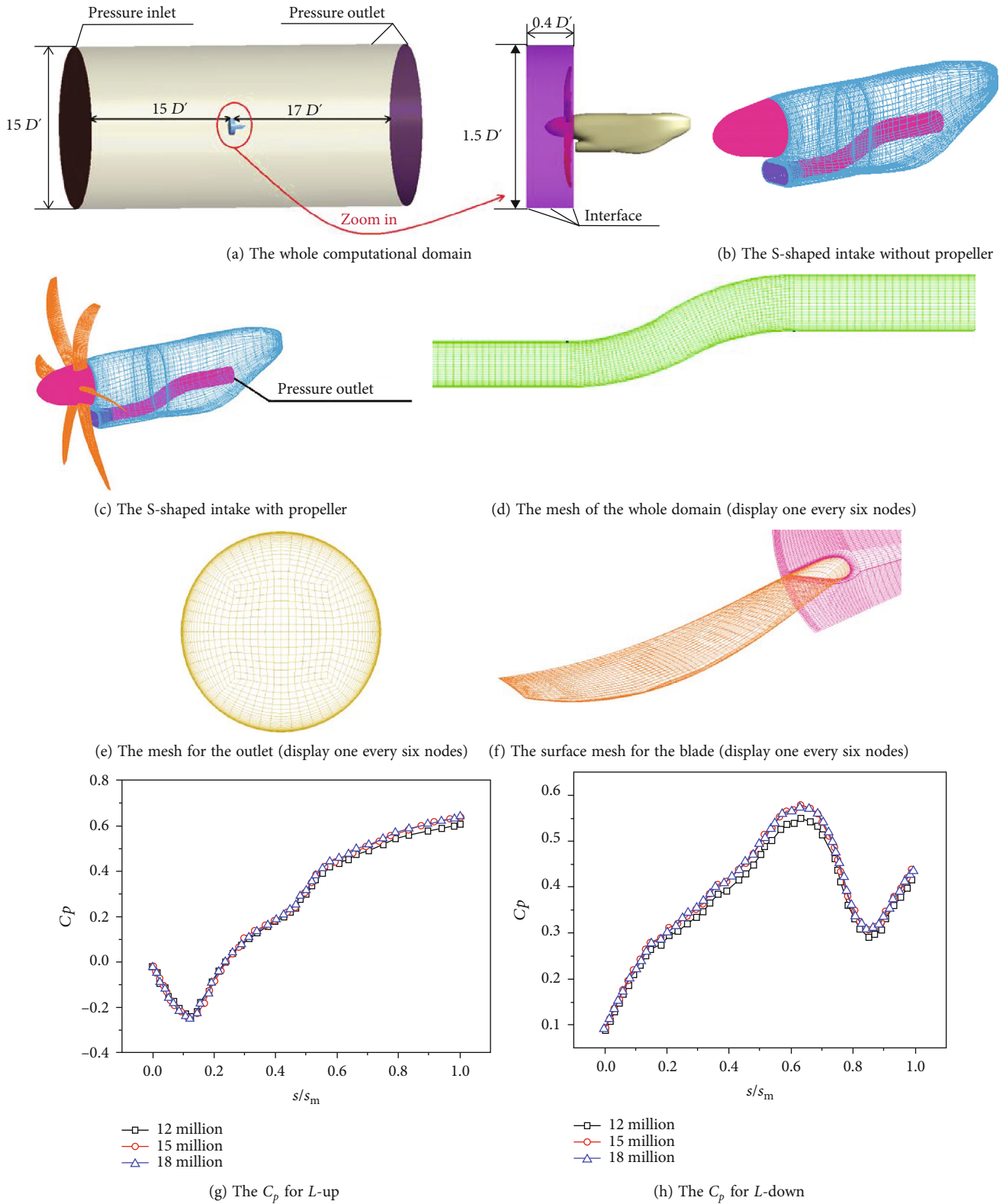


FIGURE 2: Mesh for the numerical simulation.

compressor face, but he did not consider the propeller rotation effect. Ruiz-Calavera et al. [17] carried out experimental and numerical studies on a high-offset subsonic turboprop intake. They employed two commercial codes (ANSYS Flu-

ent and ANSYS CFX) to simulate the flow field in the intake. By comparing the numerical results with the experimental results, they showed that the two numerical methods are in good agreement with the experimental results and the propeller

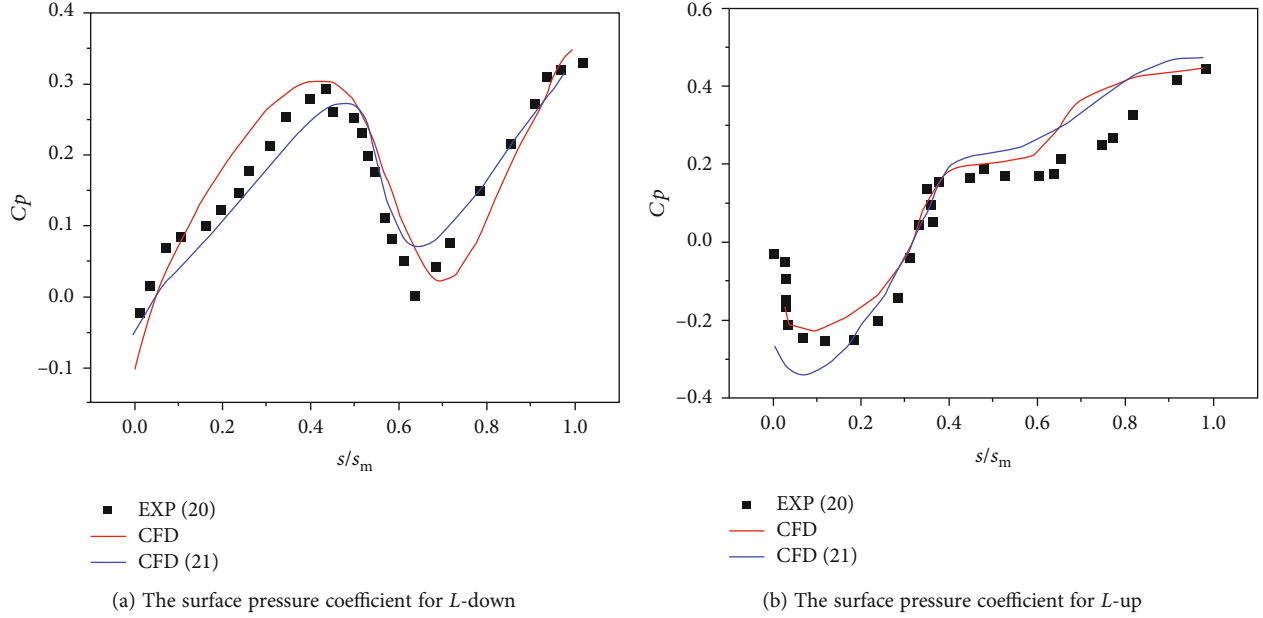


FIGURE 3: Comparisons between simulated results and experimental (EXP [20]).

TABLE 2: The cases for the numerical simulation.

Location case	Rotation speed of the propeller $n$ (rpm)
Case 1 (propeller-off)	
Case 2 (propeller-on)	800
Case 3 (propeller-on)	900
Case 4 (propeller-on)	1000
Case 5 (propeller-on)	1100
Case 6 (propeller-on)	1200
Case 7 (propeller-on)	1300

rotation effect has strong effect on the flow field in the intake, but the propeller slipstream effect on the flow field (such as flow separation and secondary flow) is not studied in detail. What are the propeller slipstream effects on flow separation and secondary flow in S-shaped intake? How does the airflow total pressure change with time as the blades sweep through the

intake? What is the effect of propeller rotation speed on the airflow total pressure? These problems play an important guiding role in the design of turboprop engine intake.

In the present paper, a numerical investigation for S-shaped intake with/without propeller is performed to explore the propeller slipstream influence on the flow field in the S-shaped intake. By comparing the flow field in the S-shaped intake with/without propeller, the propeller slipstream effects on flow separation and secondary flow have been discussed in detail. The effects of propeller rotation speed on the airflow total pressure loss and distortion have been given.

## 2. Computational Setup

**2.1. Model in Study.** The geometric model studied in this paper is a turboprop engine intake, as shown in Figure 1, which includes propeller, nacelle, and S-shaped intake. The main geometric dimensions are given in Table 1.

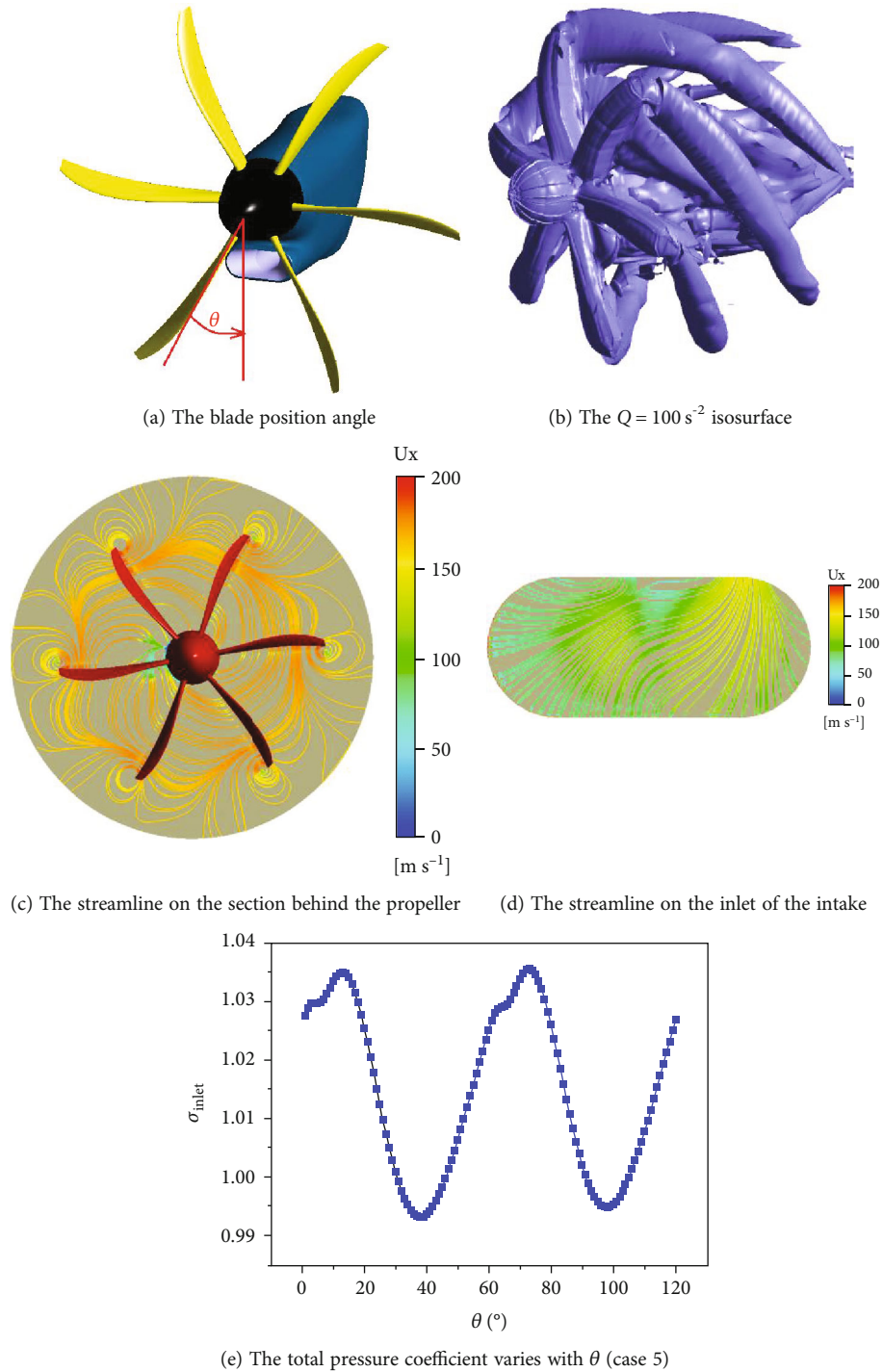


FIGURE 4: The total pressure coefficient at the inlet of the intake.

A similar S-shaped intake was provided by AIAA PAW01 and tested in ONERA wind tunnel R4MA (Modane-Avrieux, France) in 2006 [18]. Additionally, Harloff et al. [19] carried out an experimental test on a similar S-shaped intake at the NASA Lewis Research Center in the 1990s. As shown in Figure 1(c), the centerline of the S-shaped intake is composed of two arcs, and each of the arcs

is 30 degrees. The inlet diameter of the S-shaped intake  $D_{\text{in}}$  is 266.3 mm, the outlet diameter of the S-shaped intake is 328 mm, the radius of the centerline is  $r_0$  1330.8 mm, the arc length of the centerline is  $5.23 D_{\text{in}}$ , the length of the S-shaped intake  $L$  is  $5 D_{\text{in}}$ , the offset of the model  $H$  is  $1.35 D_{\text{in}}$ , and the distance between the AIP section and inlet of the S-shaped intake is  $5.72 D_{\text{in}}$ . The detailed information

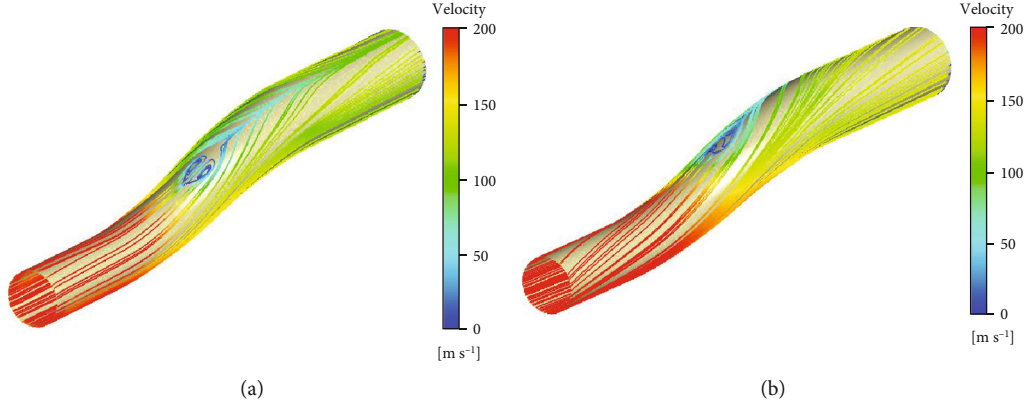


FIGURE 5: The surface limit pathline for the S-shaped intake with/without propeller.

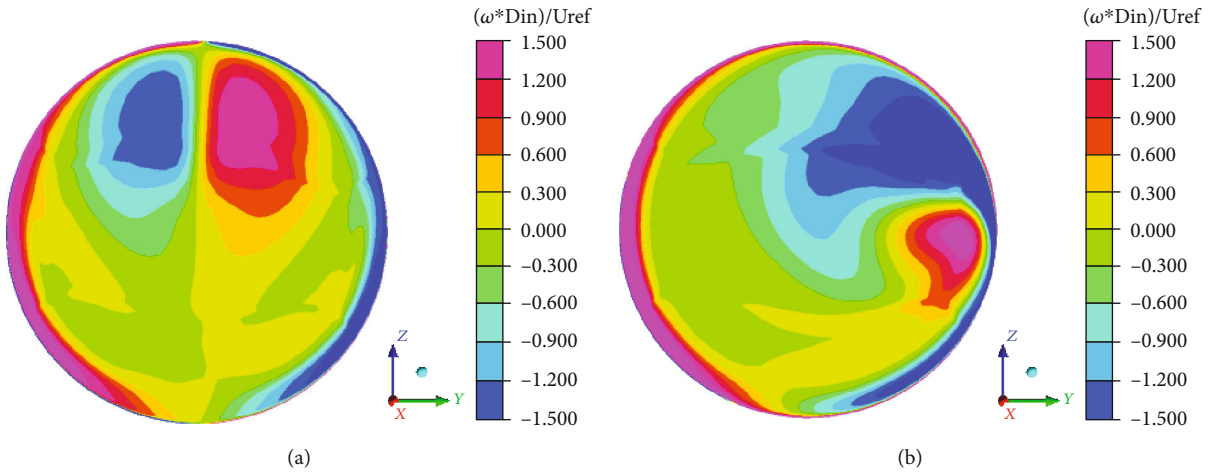


FIGURE 6: The vorticity distribution on the AIP.

of the diameter of each cross section along the  $s$  coordinate can be given by

$$\frac{D}{D_{in}} = 1 + 3 \left( \frac{D_{out}}{D_{in}} - 1 \right) \left( \frac{s}{s_m} \right)^2 - 2 \left( \frac{D_{out}}{D_{in}} - 1 \right) \left( \frac{s}{s_m} \right)^3, \quad (1)$$

in which  $s_m$  is the length of the central line, and  $s/s_m = 0$  at the center of the inlet for S-shaped intake.

The diameter of the propeller  $D'$  is 4000 mm. The distribution of chord length  $b_r$  and torsion angle  $\psi$  for the blade is shown in Figures 1(d) and 1(e).

**2.2. Numerical Method and Validation.** ANSYS Fluent 16.0 is employed to perform a numerical simulation for the flow field in S-shaped intake. In the simulation, the unsteady compressible Reynolds-averaged Navier-Stokes (RANS) equations are solved with a finite volume method. The SST  $k-\omega$  model is employed for the numerical simulation. The method of sliding grid is used to simulate the propeller rotation, and the time step is  $\tau/360$  ( $\tau$  is the rotation period of the propeller). The numerical simulation is carried out on a computer with 32 G memory, and every case is completed

in about one week. The simple algorithm is used to deal with pressure-velocity coupling. The convection terms are discretized by second-order upwind scheme, and the diffusion terms are discretized by second-order central difference scheme.

The whole computational domain is a cylinder, the diameter of the computational domain is  $15D'$ , the distance between the inlet of the computational domain and the rotating plane of the propeller is  $15D'$ , and the distance between the outlet of the computational domain and the rotating plane of the propeller is  $17D'$  (Figure 2(a)). The whole calculation domain is divided into rotating domain surrounding the propeller and stationary domain. The diameter of rotating domain is  $1.5D'$ . According to the surrounding atmospheric condition ( $P_0 = 56660.4$  Pa and  $T_0 = 249$  K) of an aircraft cruising ( $Ma = 0.527$ ) at an altitude of 6000 m, the pressure inlet boundary condition was chosen for the inlet of computational domain and total pressure was given ( $P_0 = 56660.4$  Pa) (Figure 2(a)). The pressure outlet boundary condition was chosen for the outlet of computational domain, and the pressure was given ( $P_{outlet} = 47217$  Pa) (Figures 2(a) and 2(c)). The cylindrical surface surrounding

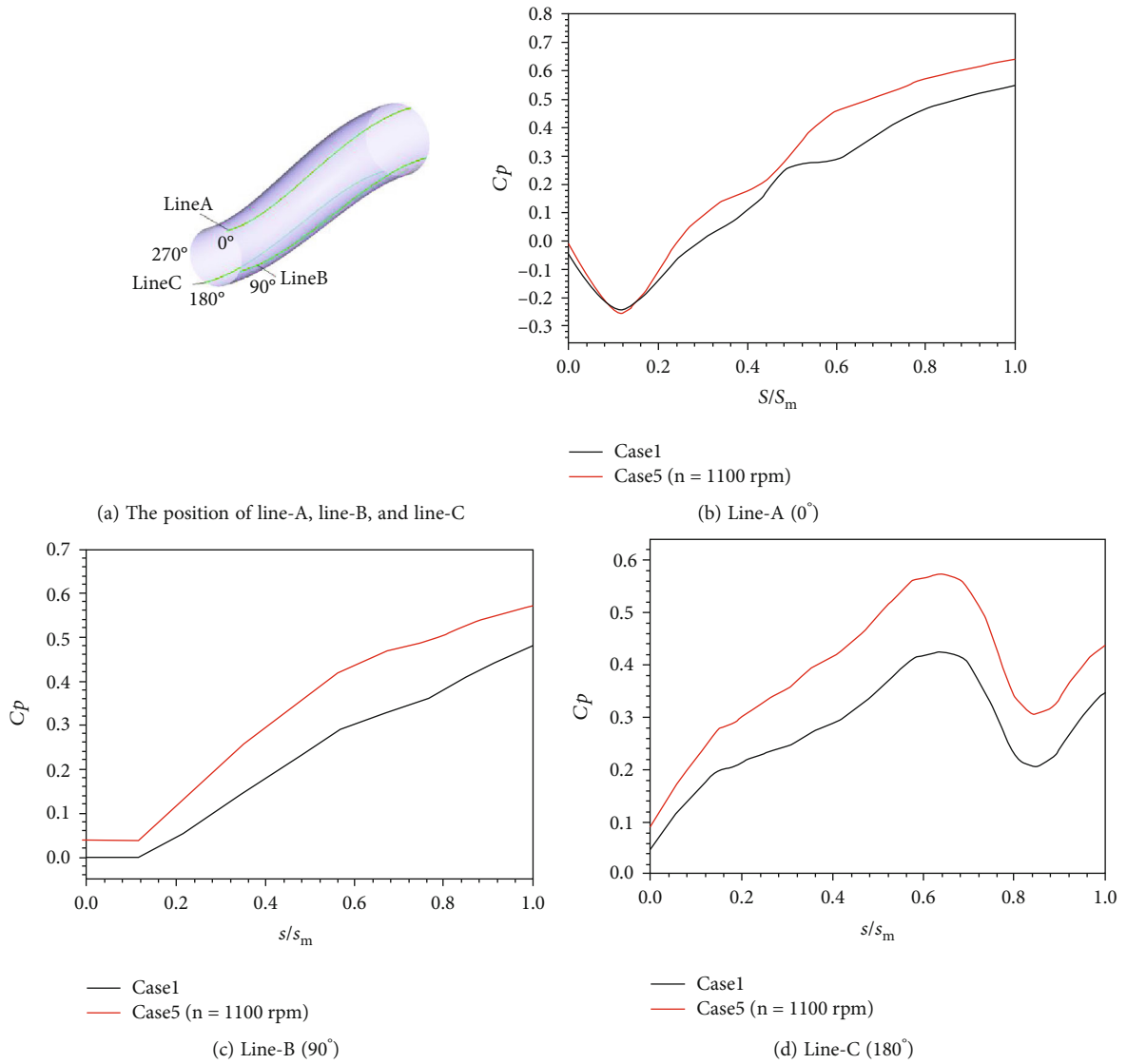


FIGURE 7: The surface pressure coefficient for the S-shaped intake with/without propeller.

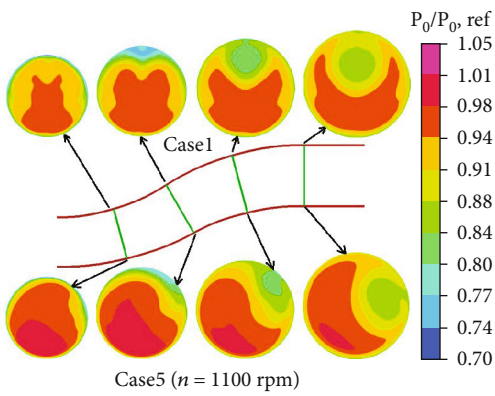


FIGURE 8: Contour of total pressure.

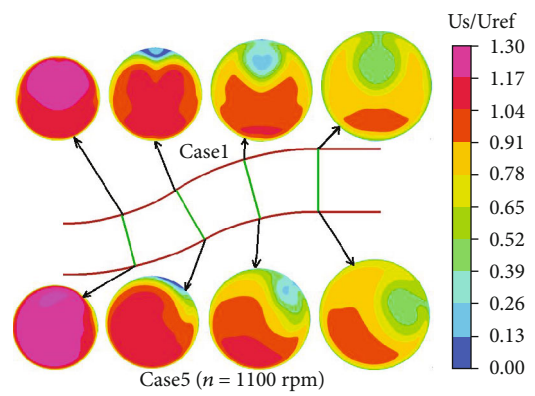


FIGURE 9: Contour of streamwise velocity.

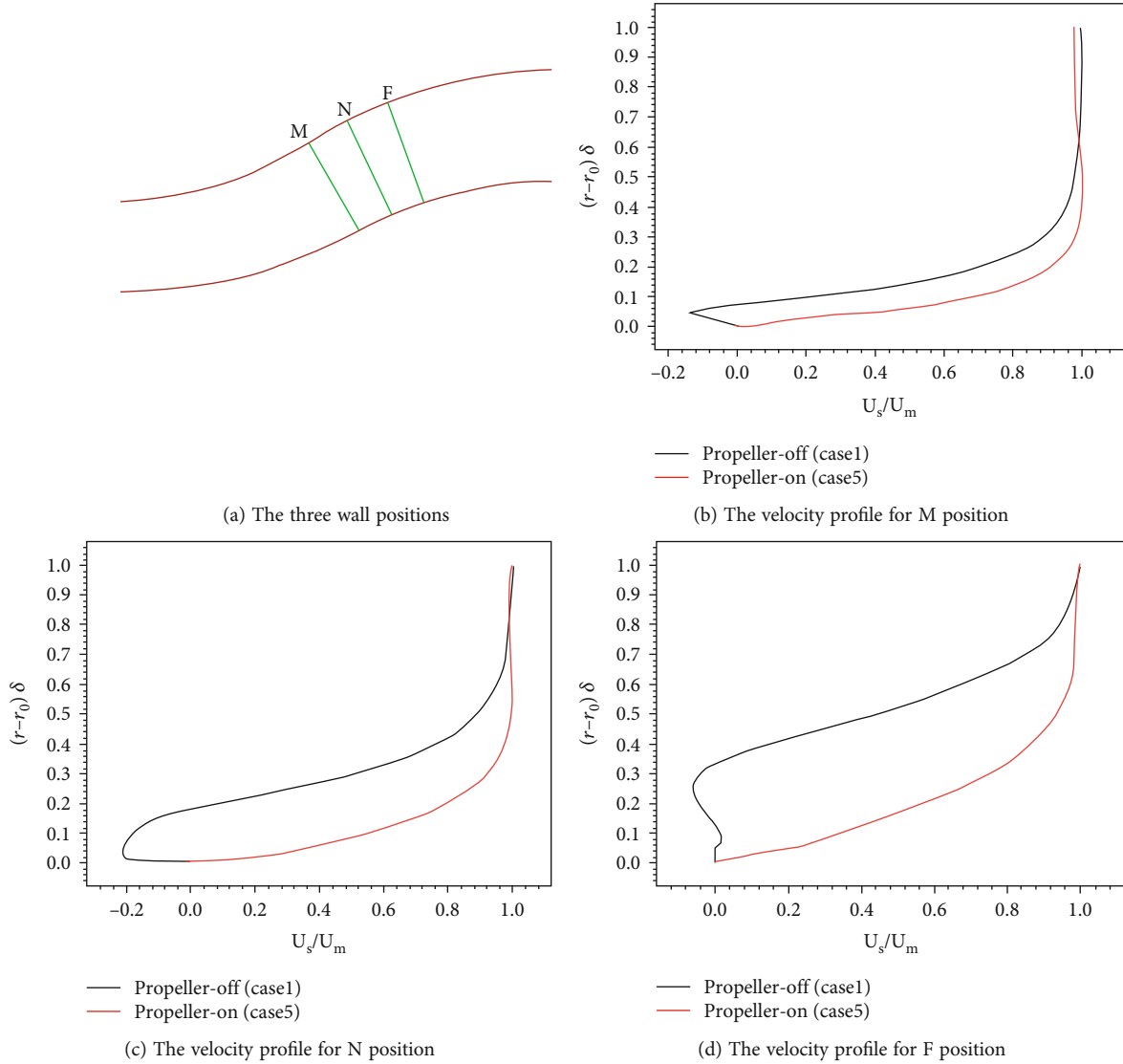


FIGURE 10: Velocity profile for different positions.

the propeller was set as the interface (Figure 2(a)). No-slip adiabatic wall boundary condition was chosen for the wall.

The mesh for the simulation was generated in the ANSYS ICEM16.0. The surface mesh for propeller, nacelle, and intake is shown in Figure 2. In order to verify the independence of grid number for the numerical simulation, three grids (12 million, 15 million, and 18 million, respectively) were employed to simulate the S-shaped intake with propeller ( $n = 1100$  rpm), as shown in Figures 2(g) and 2(h). The difference between the three grids is that the grid of the S-shaped intake part. The coarse grid (12 million) was generated with the limitations of the first grid layer ( $y^+ \approx 1$ ) and spatial grid growth ratio of 1.1. The medium (15 million) and fine (18 million) grids were generated based upon the coarse grid. Figures 2(g) and 2(h) show the surface pressure coefficient  $C_p$  for S-shaped intake, and  $C_p$  is calculated by the following formula:

$$C_p = \frac{P - P_{\text{ref}}}{1/2 \rho U_{\text{ref}}^2}, \quad (2)$$

in which  $P_{\text{ref}}$  ( $P_{\text{ref}} = 47000$  Pa) and  $U_{\text{ref}}$  ( $U_{\text{ref}} = 167$  m/s) are the averaged pressure and velocity on the cross section ( $s/s_m = 0$ ). It can be seen from Figures 2(g) and 2(h) that  $C_p$  obtained by the medium grid (15 million) and fine grid (18 million) basically coincides with negligible error. Therefore, the medium grid (15 million) was selected to simulate for the S-shaped intake with/without propeller. The number of grid nodes for the intake part was 6 million, about 10000 nodes were arranged on each cross section, and 600 nodes were arranged in the main flow direction.

To verify the numerical method, a simulation of S-duct [20, 21] was carried out as shown in Figure 3. The surface pressure coefficient for the S-duct is compared with

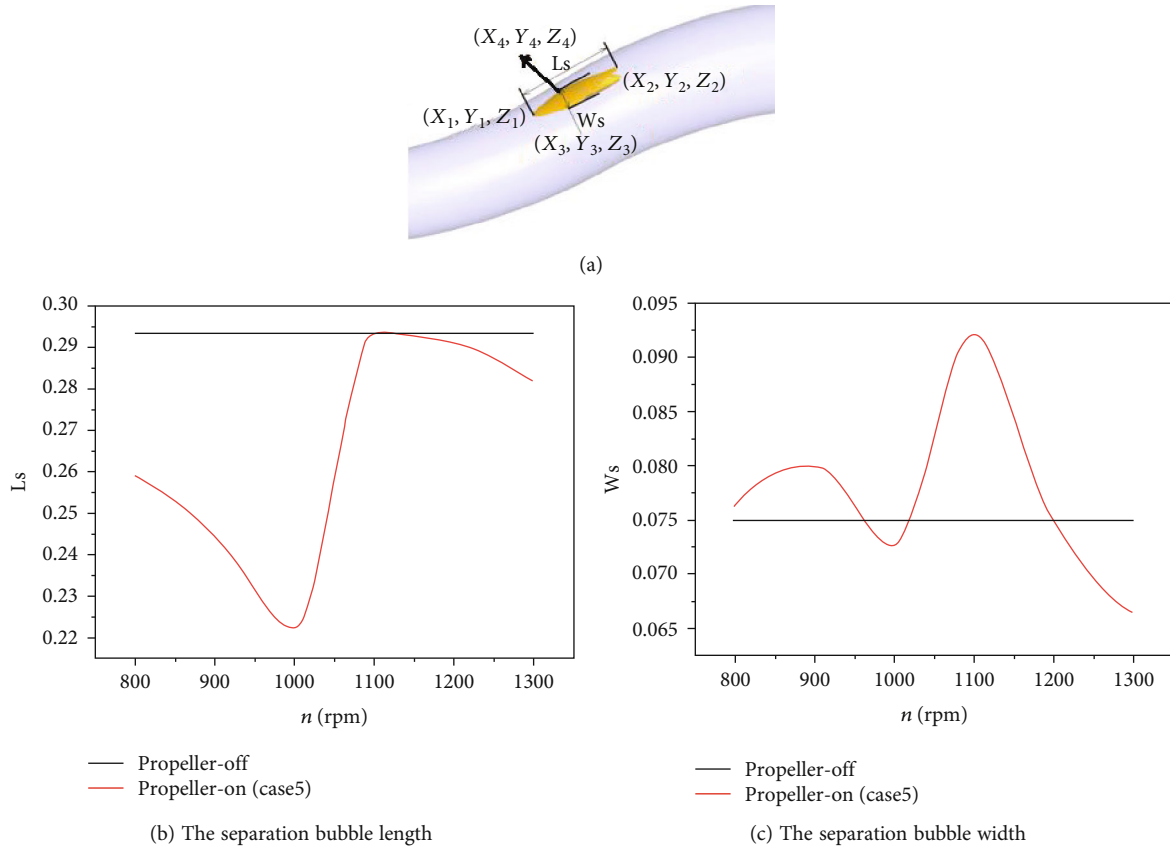


FIGURE 11: Length and width of separation bubble.

experimental results. It can be seen that there are some small deviations between the computed results and the experimental results, but the main trends are in good agreement. For the  $L$ -down, the numerical results are in good agreement with the experimental data (Figure 3(a)). For the  $L$ -up, there is 5 percent deviation between computed and experimental results ( $0 < s/s_m < 0.2$  and  $0.6 < s/s_m < 0.8$ ), and there is a constant pressure region ( $0.35 < s/s_m < 0.6$ ), indicating the streamwise flow separation phenomenon (Figure 3(b)). Due to the curvature effect, a pair of streamwise counter-rotating vortices is presented on the AIP (Figure 3(c)).

### 3. Computational Results

The numerical investigation for the S-shaped intake with/without propeller includes seven cases. Propeller-on represents the cases with propeller ( $n = 800$  rpm, 900 rpm, 1000 rpm, 1100 rpm, 1200 rpm, and 1300 rpm, respectively), and propeller-off represents the case without propeller (Table 2).

**3.1. Effect of Propeller Slipstream on Flow Field in the S-Shaped Intake.** As the propeller periodically pushes air into the S-shaped intake, the air through the propeller increases circumferential induced velocity and streamwise induced velocity (Figures 4(b) and 4(c)). The complex vortices induced by propeller have strong impact on the airflow at the inlet of the intake (Figure 4(d)). The total pressure coef-

ficient at the inlet of the S-shaped intake varies with the blade position angle ( $\theta$ ), which is obviously periodic. Total pressure recovery coefficient  $\sigma$  and distortion coefficient DC(60) are given by

$$\sigma = \frac{P_{0,avg}}{P_{0,ref}}, \quad (3)$$

$$DC(60) = \frac{P_{0,avg} - P_{0,60 \text{ deg}}}{q_{avg}},$$

in which  $P_{0,avg}$  is the average total pressure on a cross section,  $P_{0,ref}$  is the reference average total pressure ( $P_{0,ref} = 56660.4$  Pa),  $P_{0,60 \text{ deg}}$  is the average total pressure in the 60-degree sector that results in the lowest value, and  $q_{avg}$  is the average dynamic pressure on a cross section.

In order to understand the internal flow field structure in the S-shaped intake, the three-dimensional pathline is shown in Figure 5 and the vorticity distribution on the AIP section is shown in Figure 6. For the S-shaped intake without propeller, the pathline is symmetrical about the symmetry plane (Figure 5(a)) and a pair of counter-rotating vortices forms on the AIP (Figure 6(a)); for the S-shaped intake with propeller, the pathline is no longer symmetrical due to the propeller rotation effect, but has a certain deflection (Figure 5(b)). The secondary vortices which are consistent with the propeller rotation direction are strengthened, and the secondary

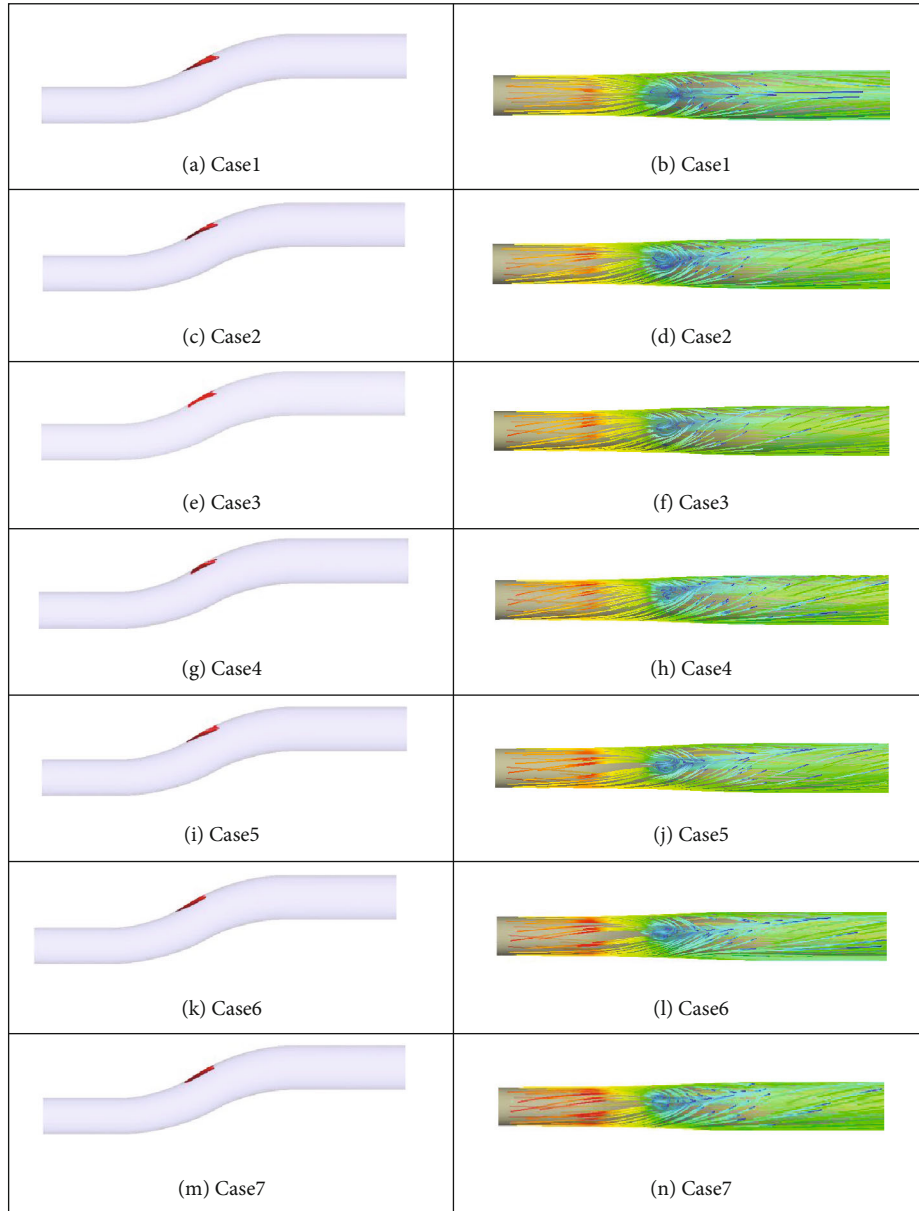


FIGURE 12: Separation bubble and the limit pathline for wall.

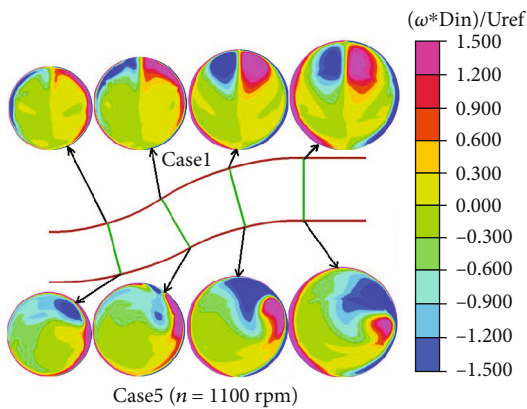


FIGURE 13: The vorticity distribution on cross section for the S-shaped intake.

vortices which are opposite to the propeller rotation direction are weakened (Figure 6(b)).

As shown in Figure 7, the wall pressure coefficient for the S-shaped intake with propeller is larger than that for the S-shaped intake without propeller. For the line-A (Figure 7(a)), the constant pressure area decreases due to the influence of propeller slipstream, which means that the propeller slipstream has restraining effect on the flow separation (Figure 7(b)); for the line-B and line-C (Figure 7(a)), the effect of propeller slipstream is only to increase the surface pressure, and the pressure change trend is the same for the S-shaped intake with/without propeller (Figures 7(c) and 7(d)).

Figures 8 and 9, respectively, show the total pressure and streamwise velocity on different cross sections. A pair of counter-rotating vortices gradually evolves downstream to a low-pressure area on the AIP section, but the low-pressure area

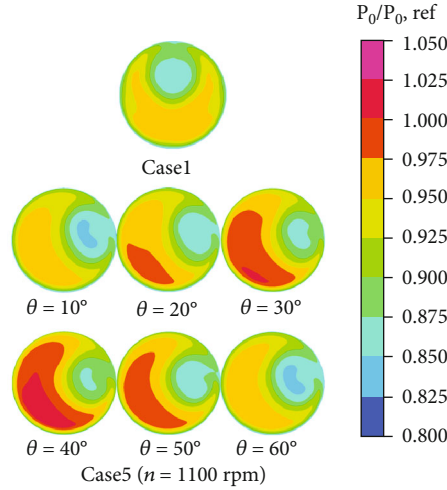
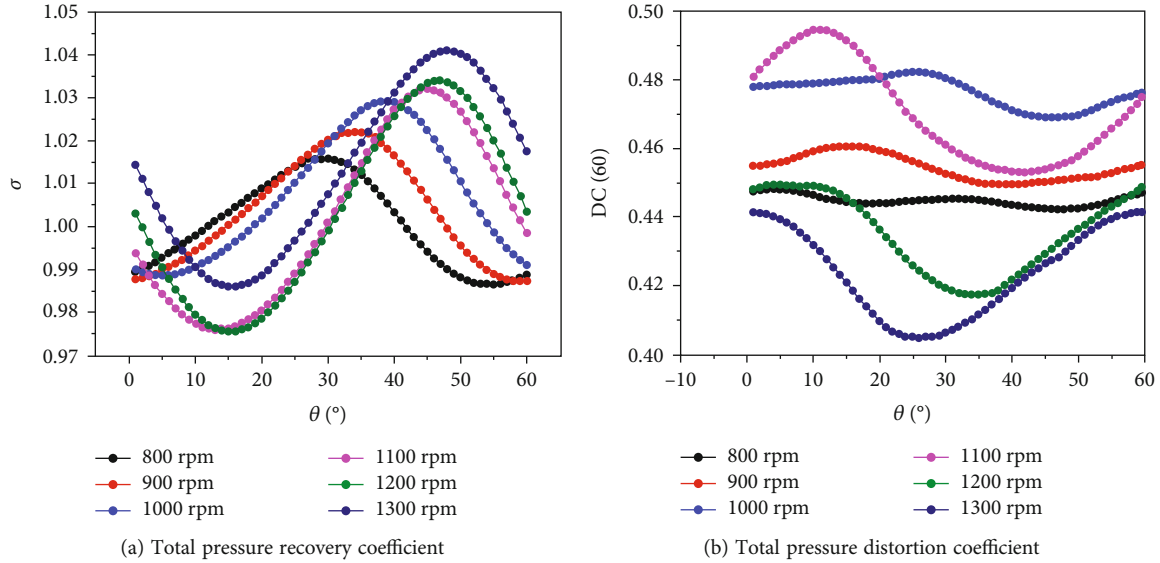

 FIGURE 14: Total pressure distribution for different blade positions ( $\theta$ ).

 FIGURE 15: Total pressure recovery coefficient and distortion coefficient vary with  $\theta$ .

TABLE 3: Total pressure recovery coefficient and distortion coefficient for different cases.

	$\lambda$	$\sigma$	DC(60)
Case 1		0.99026	0.42236
Case 2	3.13	1.00042	0.44479
Case 3	2.78	1.00352	0.45437
Case 4	2.50	1.00702	0.47633
Case 5	2.27	1.00161	0.47062
Case 6	2.09	1.00319	0.43504
Case 7	1.92	1.01463	0.42359

deflects relative to the symmetry plane due to the influence of propeller slipstream.

Due to the propeller streamwise interference on airflow, it injects energy into the low-energy fluid in the S-shaped

intake, so it has a certain inhibitory effect on streamwise flow separation in the S-shaped intake. Figure 10 shows the velocity profiles at the three wall positions (Figure 10(a)) for the S-shaped intake. The  $r - r_0/\delta$  represents the ratio of wall normal distance to boundary layer thickness, and  $U_s/U_m$  represents the ratio of streamwise velocity to the maximum velocity on the section. It can be seen from Figure 10 that there is backflow for the S-shaped intake without propeller, but not for the S-shaped intake with propeller.

Figure 11 shows the change of the separation bubble length ( $L_s$ ) and width ( $W_s$ ) with the propeller rotation speed, from which it can be seen that the separation bubble size for the S-shaped intake with propeller is smaller than that for the S-shaped intake without propeller. The separation bubble length ( $L_s$ ) and width ( $W_s$ ) have been obtained by the following formulas:

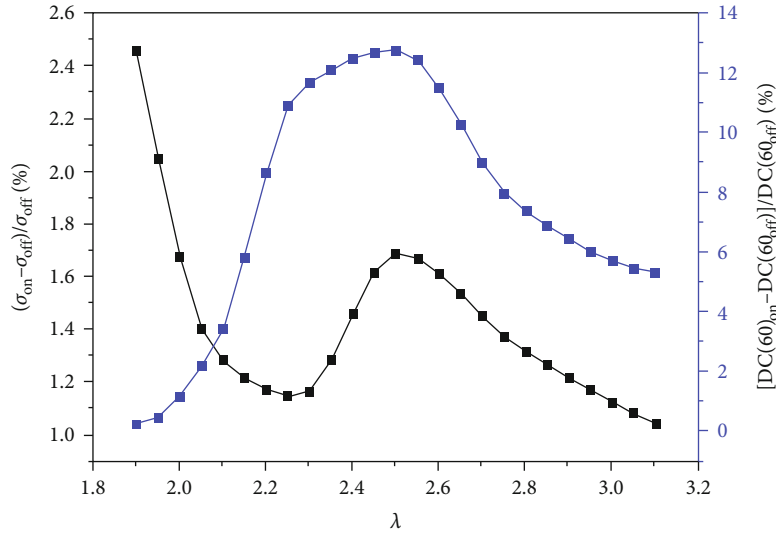


FIGURE 16: The total pressure recovery coefficient and distortion coefficient on the AIP vary with  $\lambda$ .

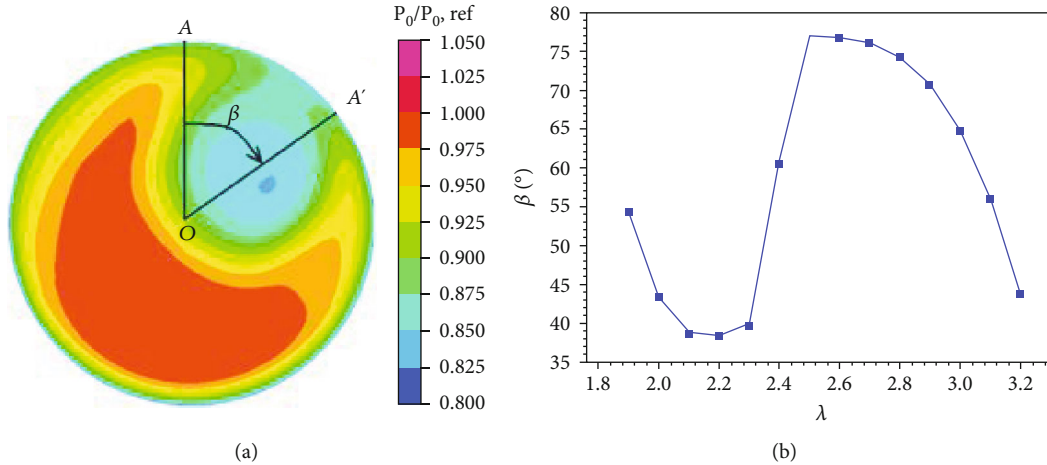


FIGURE 17:  $\beta$  varies with propeller advance ratio  $\lambda$ .

$$L_s = \sqrt{(x_1 - x_2)^2 + (y_1 - y_2)^2 + (z_1 - z_2)^2}, \quad (4)$$

$$W_s = \sqrt{(x_3 - x_4)^2 + (y_3 - y_4)^2 + (z_3 - z_4)^2},$$

in which  $(x_1, y_1, z_1)$ ,  $(x_2, y_2, z_2)$ ,  $(x_3, y_3, z_3)$ , and  $(x_4, y_4, z_4)$  are the boundary point coordinates of the separation bubble (Figure 11(a)).

For the S-shaped intake with propeller, with the increase of propeller speed, the separation bubble size first decreases (Figures 12(c), 12(e), and 12(g)), then increases (Figures 12(g) and 12(i)), and then decreases (Figures 12(i), 12(k), and 12(m)). The pathline obviously deflects in the S-shaped intake with propeller (Figures 12(d), 12(f), 12(h), 12(j), 12(l), and 12(n)), and a pair of counter-rotating vortices is no longer symmetrical about the symmetry plane due to the circumferential interference of the propeller.

As the airflow through the propeller increases circumferential induced velocity, the counter-rotating vortices in the S-shaped intake are not being symmetrical about the sym-

metry plane (Figure 13). The secondary vortices in the same direction with the propeller rotation are strengthened, and the secondary vortices in the opposite direction with the propeller rotation are weakened, which has significant impact on the airflow total pressure uniformity. Therefore, the distortion coefficient on the AIP section for the S-shaped intake with propeller is larger than that for the S-shaped intake without propeller.

**3.2. Effect of the Propeller Slipstream on  $\sigma$  and DC(60) on the AIP.** As the blades sweep through the inlet of the S-shaped intake, the flow field changes periodically with  $\theta$ . Figure 14 shows contour map of total pressure on the AIP section for different  $\theta$ , from which can be seen that total pressure changes with  $\theta$  and reaches maximum at  $\theta = 40^\circ$ .

As shown in Figure 15, the total pressure recovery coefficient and distortion coefficient on the AIP change with blade position angle ( $\theta$ ). As the blades sweep through the inlet of the S-shaped intake, the total pressure recovery coefficient and distortion coefficient change sinusoidally with  $\theta$ .

With the increase of propeller rotation speed, the amplitude also increases. There is phase difference in these curves for different propeller rotation speeds, which is caused by the pressure wave propagation.

Total pressure recovery coefficient and distortion coefficient for different cases are given by Table 3. The  $\sigma$  and DC(60) on the AIP section for the S-shaped intake with propeller are larger than those for the S-shaped intake without propeller. As can be seen from Table 3, the higher the rotation speed is, the more obvious the propeller slipstream effect is. For  $n = 1300$  rpm, the  $\sigma$  increases by 0.02437, and the DC(60) increases by 0.00123.

As shown in Figure 16, the total pressure recovery coefficient and distortion coefficient on the AIP section for the S-shaped intake vary with  $\lambda$ . For  $1.9 < \lambda < 2.3$ , the total pressure recovery coefficient decreases with  $\lambda$ , and distortion coefficient increases with  $\lambda$ ; for  $2.5 < \lambda < 3.1$ , the total pressure recovery coefficient and distortion coefficient decrease with  $\lambda$ .

As shown in Figure 17, the deflection angle  $\beta$  is the angle between  $OA'$  and  $OA$ . The line  $OA$  is the intersection line of symmetry plane and local cross section. The  $OA'$  is the centerline of low pressure area. For  $1.9 < \lambda < 2.3$ , the deflection angle  $\beta$  for low pressure area decreases with  $\lambda$ ; for  $2.3 < \lambda < 2.5$ , the deflection angle  $\beta$  for low pressure area increases with  $\lambda$ ; for  $2.5 < \lambda < 3.2$ , the deflection angle  $\beta$  for low pressure area decreases with  $\lambda$ .

#### 4. Conclusions

By comparing the flow field for the S-shaped intake with/without propeller, it is found that the propeller slipstream has strong influence on the flow field in S-shaped intake. The following conclusions can be drawn:

- (1) The propeller slipstream can increase the total pressure recovery coefficient  $\sigma$  and total pressure distortion coefficient DC(60) on the AIP section of the S-shaped intake.
- (2) The propeller slipstream can restrain the flow separation in S-shaped intake and enhance the secondary flow in the S-shaped intake.
- (3) As the blades sweep through the inlet of the S-shaped intake, the total pressure recovery coefficient and distortion coefficient on the AIP section change periodically with  $\theta$ . The amplitude and phase of the change vary with propeller rotation speed.

#### Nomenclature

$D_{in}$ :	Inlet diameter of the S-shaped intake
$D_{out}$ :	Outlet diameter of the S-shaped intake
$L$ :	Horizontal length of the S-shaped intake
$H$ :	Offset distance of the S-shaped intake
$D$ :	The cross section diameter of the S-shaped intake
$D'$ :	The diameter of the propeller
$R'$ :	The radius of the propeller

$r'$ :	Radial coordinate for the blade element
$br$ :	Chord length for the blade element
$\psi$ :	Torsion angle for the blade element
$\sigma$ :	Total pressure recovery coefficient
DC(60):	Distortion coefficient
$\sigma_{inlet}$ :	Total pressure recovery coefficient for the inlet of the S-shaped intake
$C_p$ :	Pressure coefficient
$n$ :	Rotation speed of the propeller
$\tau$ :	Rotation period of the propeller
$\lambda$ :	Advance ratio of the propeller ( $\lambda = 60U_{ref}/nD'$ )
$\theta$ :	The blade position angle
$r$ :	Radial coordinate
$s$ :	Streamwise coordinate
$s_m$ :	The length of centerline for S-shaped intake
$\omega$ :	Vorticity
$\delta$ :	Boundary layer thickness
$T_0$ :	Total temperature
$P_0$ :	Total pressure
$P_{0, inlet}$ :	Total pressure for the inlet of computational domain
$P_{0, ref}$ :	Reference average total pressure
$P$ :	Static pressure
$P_{ref}$ :	Reference average static pressure on the cross section ( $s/s_m = 0$ )
$P_{outlet}$ :	Static pressure for the outlet of computational domain
$P_{0, avg}$ :	Average total pressure on cross section
$P_{0, 60 \text{ deg}}$ :	Average total pressure in the 60-degree sector that results in the lowest value
$q_{avg}$ :	Average dynamic pressure on cross section
$U_s$ :	Streamwise velocity
$U_x$ :	Velocity in $X$ direction
$U_m$ :	The maximum streamwise velocity on cross section
$L_s$ :	Length of separation bubble
$W_s$ :	Width of separation bubble
$Ma$ :	Mach number for free stream flow
$U_{ref}$ :	Reference average velocity on the cross section ( $s/s_m = 0$ )
AIP:	Aerodynamic Interface Plane ( $0.5D_{in}$ downstream of the outlet for S-shaped intake).

#### Data Availability

All data used to support the findings of this study are included within the article.

#### Conflicts of Interest

The authors declare that they have no conflicts of interest.

#### References

- [1] M. Tormalm, "Design and analysis of compact UAV ducts," in *24th AIAA Applied Aerodynamics Conference*, San Francisco California, 2006.

- [2] S. Kamali, B. Reza Ahrabi, R. S. Webster, and K. Sreenivas, "Numerical simulation of compressible flow in a diffusing S-duct with and without vortex generators," in *33rd AIAA Applied Aerodynamics Conference*, Dallas, TX, 2015.
- [3] G. A. Gerolymos, S. Joly, M. Mallet, and I. Vallet, "Reynolds-stress model flow prediction in aircraft-engine intake double-S-shaped duct," *Journal of Aircraft*, vol. 47, no. 4, pp. 1368–1381, 2012.
- [4] M. Johansson, "Propulsion integration in an UAV," in *24th AIAA Applied Aerodynamics Conference*, San Francisco California, 2006.
- [5] A. Kirk, A. Kumar, J. Gargoloff, O. Rediniotis, and P. Cizmas, "Numerical and experimental investigation of a serpentine inlet duct," in *45th AIAA Aerospace Sciences Meeting and Exhibit*, Guangzhou, China, 2007.
- [6] B. H. Anderson, D. R. Reddy, and K. Kapoor, "Study on computing separating flows within a diffusion inlet S-duct," *Journal of Propulsion and Power*, vol. 10, no. 5, pp. 661–667, 1994.
- [7] S. R. Wellborn, B. A. Reichert, and T. H. Okiishi, "Study of the compressible flow in a diffusing S-duct," *Journal of Propulsion and Power*, vol. 10, no. 5, pp. 668–675, 1994.
- [8] B. J. Wendt and B. A. Reichert, "Vortex ingestion in a diffusing S-duct inlet," *Journal of Aircraft*, vol. 33, no. 1, pp. 149–154, 1996.
- [9] M. J. Brear, Z. Warfield, J. F. Mangus, C. S. Braddom, J. D. Paduano, and J. S. Philhower, "Flow separation within the engine inlet of an uninhabited combat air vehicle (UCAV)," *Journal of Fluids Engineering*, vol. 126, no. 2, pp. 266–272, 2004.
- [10] G. J. Harloff, C. F. Smith, J. E. Bruns, and J. R. Debonis, "Navier-Stokes analysis of three-dimensional S-ducts," *Journal of Aircraft*, vol. 30, no. 4, pp. 526–533, 1993.
- [11] B. Berrier and B. Allan, "Experimental and computational evaluation of flush-mounted, S-duct inlets," in *42nd AIAA Aerospace Sciences Meeting and Exhibit*, Reno, Nevada, 2004.
- [12] J. Foster, B. J. Wendt, B. A. Reichert, and T. H. Okiishi, "Flow through a rectangular-to-semiannular diffusing transition duct," *Journal of Propulsion and Power*, vol. 13, no. 2, pp. 312–317, 1997.
- [13] C. Fiola and R. K. Agarwal, "Simulation of secondary and separated flow in diffusing S ducts," *Journal of Propulsion and Power*, vol. 31, no. 1, pp. 180–191, 2015.
- [14] D. Gil-Prieto, D. G. MacManus, P. K. Zachos, G. Tanguy, F. Wilson, and N. Chiereghin, "Delayed detached-eddy simulation and particle image velocimetry investigation of S-duct flow distortion," *AIAA Journal*, vol. 55, no. 6, pp. 1893–1908, 2017.
- [15] B. Little and T. JR, "An experimental investigation of S-duct diffusers for high-speed propfans," in *AIAA/SAE/ASME 18th Joint Propulsion Conference*, Cleveland, Ohio, 1982.
- [16] P. L. McDill, "S-duct inlet/diffusers for turboprop offset gearbox applications," in *AIAA/ASME/SAE/ASEE 22nd Joint Propulsion Conference*, Huntsville, Alabama, 1986.
- [17] L. Ruiz-Calavera, D. Funes-Sebastian, and D. Perdones-Diaz, "Powered model wind tunnel tests of a high-offset subsonic turboprop air intake," in *46th AIAA/ASME/SAE/ASEE Joint Propulsion Conference & Exhibit*, Nashville, TN, 2010.
- [18] L.-M. Gea, "CFD simulation for S-duct test case using overset grids," in *49th AIAA/ASME/SAE/ASEE Joint Propulsion Conference*, San Jose, CA, 2013.
- [19] G. Harloff, B. Reichert, and S. Wellborn, "Navier-Stokes analysis and experimental data comparison of compressible flow in a diffusing S-duct," in *10th Applied Aerodynamics Conference*, Palo Alto, CA, 1992.
- [20] A.-L. Delot, E. Garnier, and D. Pagan, "Flow control in a high-offset subsonic air intake," in *47th AIAA/ASME/SAE/ASEE Joint Propulsion Conference and Exhibit*, San Diego, CA, USA, 2011.
- [21] B. Reza Ahrabi, K. Sreenivas, and R. S. Webster, "Computational investigation of compressible flow in a diffusing S-duct," in *49th AIAA/ASME/SAE/ASEE Joint Propulsion Conference*, San Jose, CA, 2013.